Field-Aligned Current Response to Solar Indices

R. Edwards, Thom ; Weimer, D. R. ; Tobiska, W. K. ; Olsen, Nils

Published in:
Journal of Geophysical Research

Link to article, DOI:
10.1002/2016ja023563

Publication date:
2017

Document Version
Peer reviewed version

Field-Aligned Current Response to Solar Indices

Thom R. Edwards[1], D. R. Weimer[1], W. K. Tobiska[2], Nils Olsen[3]

Thom R. Edwards, hardsnow@vt.edu

[1]Space@VT, Virginia Tech, Blacksburg, Virginia, USA

[2]Space Environment Technologies

[3]DTU Space, Technical University of Denmark

This article has been accepted for publication and undergone full peer review but has not been through the copyediting, typesetting, pagination and proofreading process, which may lead to differences between this version and the Version of Record. Please cite this article as doi: 10.1002/2016JA023563

Abstract. Magnetometer data from three satellite missions have been used to analyze and identify the effects of varying solar radiation on the magnitudes and locations of field-aligned currents in the Earth's upper atmosphere. Data from the CHAMP, Ørsted, and Swarm satellite missions have been bought together to provide a database spanning a 15 year period. The extensive time frame has been augmented by data from the ACE satellite, as well as a number of indices of solar radiation. This data set has been sorted by a number of solar wind, interplanetary magnetic field, and solar radiation indices to provide measurements for the field-aligned current structures in both hemispheres for arbitrary seasonal tilts. In addition, routines have been developed to extract the total current for different regions of the current structures, including regions 0, 1, and 2. Results from this study have been used to evaluate the effects of variations in four different solar indices on the total current in different regions of the polar cap. While the solar indices do not have major influence on the total current of the polar cap when compared to solar wind and interplanetary magnetic field parameters it does appear that there is a nonlinear response to increasing $F_{10.7}$, $M_{10.7}$, and $S_{10.7}$ solar index. Surprisingly, there appears to be a very linear response as $Y_{10.7}$ solar index increases.

Keypoints:

- Field-aligned current does not always have a linear relationship to increasing solar index.

- A new method of field-aligned current region identification and totaling has been developed.
- The summer hemisphere draws current away from the winter hemisphere.

1. Introduction

Understanding the terrestrial response to the solar wind and embedded interplanetary magnetic field (IMF) is paramount to being able to forecast and predict major solar storms and their impact on our planet. A key part of this interaction is the structure and strength of the field-aligned current (FAC) systems in the polar caps during different space weather conditions. These FACs, in turn, complete the circuit between the magnetosphere and the ionosphere, and allow energy to be dissipated into the neutral atmosphere.

This connection can cause magnetospheric perturbations and currents which have been shown to be the cause of a number of effects outside of the atmosphere, including geomagnetically induced currents on man-made structures such as power grids, railways, and other long distance conducting structures [*Lanzerotti and Gregori*, 1986; *Boteler et al.*, 1998; *Bolduc*, 2002; *Gummow*, 2002]. In addition, Joule heating of the thermosphere can have undesired effects on satellites in low Earth orbits. The currents that generate these effects can be quite large, totaling approximately 4 MA for typical solar wind and IMF conditions and increasing as more extreme driving occurs [*Weimer*, 2005a]. Parameterizing the changes and the current flowing in the ionosphere is of great importance for understanding the system as a whole.

Part of this parameterization depends on the separation of current into different regions relative to the pole, commonly referred to as Region 0 (R0) for the poleward most systems, Region 1 (R1) for the systems next highest in latitude, and Region 2 (R2) for the lowest latitude systems. The Region 1 and Region 2 systems were initially observed and classified by *Iijima and Potemra* [1976a, b] as a pair of concentric "rings" of current in the polar

ionosphere using TRIAD magnetometer data. Region 1 currents flow in to the ionosphere on the dawn side and out on the dusk side. Region 2 currents do the opposite, flowing out of the ionosphere on the dawn side and into the ionosphere on the dusk side.

Region 1 current systems have been shown to map to the outer portions of the of the Earth's magnetosphere, particularly the magnetopause and the outer portions of the plasma sheet [*Cowley*, 2000; *Carter et al.*, 2016]. Region 2 current systems are generally considered to close with the partial ring current. Region 0 current systems, first noted by *Iijima and Potemra* [1976b], are poleward of the Region 1 systems and are generally associated with day side cusp region of the magnetosphere. The structure of Region 0 systems have been shown to be highly dependent on the IMF B_y strength [*Ganushkina et al.*, 2015].

As further investigation into these current systems have developed it was found that the current regions are much more complex and are highly dependent on IMF and solar wind drivers [*Ganushkina et al.*, 2015]. The direction and strength of the IMF is of particular importance. Current systems tend to increase in strength and move to lower latitudes as the magnitude of the IMF increases and the direction the IMF moves southward [*Carter et al.*, 2016]. Variations in axial tilt have also been found to have implications on current strength, where hemispheres in summer have increased current magnitudes [*Coxon et al.*, 2016].

Understanding the individual impact of different drivers of these current systems is important for understanding the system as a whole, and for modeling the ionosphere and magnetosphere and their impact on the planet. The role of solar radiation with ionosphereic conductivity and its relationship with FACs has been studied in the context of

seasonal variations, such as in [*Coxon et al.*, 2016], but investigations into the relationship between solar flux indices and FACs have been lacking. It is anticipated that there is some relationship between solar flux index and ionospheric conductivity, and this anticipation is the primary interest of this investigation.

Commonly the $F_{10.7}$ solar radio flux index is used to provide a proxy for the solar radiation that interacts with the Earth's atmosphere, particularly the ionosphere. The $F_{10.7}$ index, from hereon referred to as F_{10}, is based on a ground-based radio observatory and is provided as a daily average in "solar flux units" (sfu), given in units of W m^{-2} Hz^{-1} [*Bowman et al.*, 2008]. One major issue with this index, as demonstrated by *Bowman et al.* [2008], is that the 10.7-cm wavelength is not readily absorbed by the atmosphere and thus is not a good measure of the solar flux that is being absorbed by the ionosphere. In order to remedy this issue, three additional solar indices were introduced by *Tobiska et al.* [2008]; *Bowman et al.* [2008]; S_{10}, M_{10}, and Y_{10}, (using the same short-hand terminology used by *Bowman et al.* [2008]).

S_{10} is based on the Solar and Heliospheric Observatory (SOHO) and the Geostationary Operation Environmental Satellite (GOES) 12 and forward satellites, utilizing instruments that measure emissions in the 26-34 nm range. This is particularly focused on the extreme ultraviolet (EUV) that originates primarily from solar active regions. M_{10} is derived using a series of NOAA satellites equipped with the Solar Backscatter Ultraviolet (SBUV) spectrometer. This index is particularly focused on the mid-ultraviolet (MUV) radiation near 280 nm. Y_{10} is derived using a mix of two other solar indices X_{10} and Lyman-α measurements on a number of solar focused satellite missions. The X_{10} index is based on the GOES X-ray Spectrometer (XRS) with the flare component removed, while the

Lyman-α portion of the Y_{10} index is derived primarily from the SOLar STellar Irradiance Comparison Experiment (SOLSICE) and Solar EUV Experiment (SEE) instruments. The SOLSICE instrument is aboard the Upper Atmosphere Research Satellite (UARS) and the SOlar Radiation and Climate Experiment (SORCE) satellites. The SEE instrument is aboard the Thermosphere Ionosphere Mesosphere Energetics and Dynamics (TIMED) satellite. The mix of these measurements is weighted such that the X_{10} index is dominant during solar maximum, while the Lyman-α portion is dominant during solar minimum. The three supplemental indices S_{10}, M_{10}, and Y_{10} are all normalized and converted to the standard solar flux units though linear regression with F_{10}. More information about these indices is provided by *Tobiska et al.* [2008], *ISO 14222* [2013], *Tobiska et al.* [2012], and *Rees et al.* [2012].

This paper intends to demonstrate the influences that solar radiation has over FAC structure and current strength, with particular interest in extending analysis beyond just the F_{10} index. While the four solar indices are used together by [*Bowman et al.*, 2008] in an empirical formula to predict the temperature of the thermosphere, in the analysis presented here each solar index is used independently of each other.

2. Data Preparation

The data used to determine the FAC structures was obtained from the CHAallenging Minisatellite Payload (CHAMP), Ørsted, and Swarm satellite missions. In each mission, the data from the available fluxgate magnetometer was used.

The CHAMP satellite was launched in July 2000. The satellite maintained a close to circular orbit at 87° inclination, and had an initial altitude of 454 kilometers. This mission

lasted until September 2010 [*Reigber et al.*, 2002]. The data from this mission used in this investigation starts on May 15th, 2001, and ends on September 2nd, 2010.

The Ørsted satellite was launched in February of 1999. The orbit had an inclination at 96.5° and had an initial altitude of 650-860 kilometers. This mission provided magnetometer measurements up through May of 2011 [*Thomsen and Hansen*, 1999]. The data from this mission used in this investigation starts on March 15th, 1999, and ends on August 26th, 2005.

The Swarm mission includes three identical satellites, launched in November 2013 with an expected lifetime of at least 4.5 years [*Olsen et al.*, 2013]. Two of the satellites were launched at an altitude of 450 kilometers and maintained an 87.4° inclination, while the third launched at an altitude of 530 kilometers and maintained an 88° inclination. The Swarm data starts on November 26th, 2013, and data through August 17th, 2015 has been incorporated into this investigation.

Each data set was preprocessed in order to bring all three sets of magnetometer data together in to one compiled database to be used to derive the field-aligned current model. As each data set has small differences in formatting or data, specific routines to handle data mission by mission were developed to make each data set directly comparable to each other. The process is described in this section.

The data from each satellite were rotated from its original coordinate frame to a North-East-Center (NEC) frame. In some cases data were provided in the NEC frame directly as a data product, which was used when available. The locations of each point from all three missions were transformed from an Earth centered latitude and longitude to a magnetic apex coordinate system using the Definitive Geomagnetic Reference Field (DGRF) model

for data before 2015, and the International Geomagnetic Reference Field (IGRF) for during or after 2015. The location in this frame is determined by tracing the magnetic field line from the magnetic field model that intersects with the satellite location at each point to the line's highest altitude, the magnetic apex [*Richmond*, 1995; *VanZandt et al.*, 1972]. This location is then traced back on to a sphere of one Earth radius using a simple dipole model. Based on the corrected geomagnetic longitude and the timestamp of each data point, the magnetic local time (MLT) is also determined.

After rotation to a corrected geomagnetic frame, the data from each satellite was then broken into hemispherical passes terminating at the Earth's magnetic equator based on the appropriate magnetic field model. The background geomagnetic field based on this model was then subtracted for each point in the polar pass, which provides the measured difference in the magnetic field based on external drivers, which will hereon be referred to as $\Delta\mathbf{B}$.

Both the reference field models and satellite measurements have either fitting errors or measurement errors, respectively. Further processing was done to correct each magnetic field component in such a way that accounted for these errors. Using each hemispherical satellite pass separately, a linear function of the $\Delta\mathbf{B}$ data was fit using only the low latitude portions of each pass outside the auroral region. This fit was then subtracted from the entire hemispherical pass separately for each vector component. It was decided in this case that anything less than or equal to 50 degrees corrected geomagnetic latitude was outside the region of interest. An example result of this splitting and processing can be seen in Figure 1.

With the $\Delta\mathbf{B}$ data corrected and processed, the coordinate frame for each point is rotated from the NEC frame to an orthogonal system where one vector component is in the direction of the IGRF magnetic field, one vector component is in the sunward direction, and the last vector component is in the dawn-dusk direction. After latitude selection and preprocessing, the Ørsted data set included 31537 passes, the CHAMP data set included 104636 passes, and the Swarm data set included 49986 passes between the three satellites, totaling 186159 polar satellite passes with good magnetometer measurements. In addition to the sheer volume of data, the CHAMP, Ørsted, and Swarm mission satellites had considerably better attitude stability and accuracy compared to the DE-2 data used in previous models [*Weimer*, 2005b].

Similar to previous models, particularly the 2005 Weimer model, the solar wind and IMF conditions were associated with each magnetometer measurement by appropriately delaying measurements from satellite missions upwind of the bow shock [*Weimer*, 2005b]. In this study the ACE data set was used for IMF and solar wind conditions. This data set proved to be well suited for this study, as it had data for many more extreme parameter conditions compared to the IMP 8 and ISEE 3 data sets used in previous Weimer models, as well as having an extensive temporal coverage.

In addition to the solar wind and IMF conditions, the solar index value at each magnetometer measurement is also associated using the solar index data provided by Space Environment Technologies. This allows each data point to be selected for a single solar index independently of the other indices. The solar index values are considered as one of the driving conditions of the system, similar to IMF clock angle, seasonal tilt, or solar wind electric field.

Even after the magnetometer data has been processed, other errors may still be present due to processing issues, data product issues, or other unknown causes. During development of this analysis it was found that some data points had $\Delta\mathbf{B}$ magnitude values that were 3 or more orders of magnitude higher than expected. These points where the Delta-B results seemed to contain errors did not occur with any consistent pattern regarding spatial location, time, satellite mission, or other physical parameters. The most likely cause of these discrepancies are due to numerical errors that occur during frame rotations of the magnetic field vectors, but it is not certain that this is the only cause of these discrepancies. We note that small errors in the reported spacecraft attitude may result in significant offsets following the subtraction of the reference magnetic field model.

3. Derivation of FAC from $\Delta\mathbf{B}$

The technique for deriving the FAC structure from the preprocessed $\Delta\mathbf{B}$ begins by assuming a curvilinear coordinate system with three orthogonal unit vectors $\mathbf{e_1}$, $\mathbf{e_2}$, and $\mathbf{e_3}$. The current in this system is assumed to flow in one direction,

$$\mathbf{J} = J\mathbf{e_1}. \tag{1}$$

The current is then related to the magnetic field perturbations using Ampere's Law:

$$\mu_0\mathbf{J} = \nabla \times \Delta\mathbf{B}, \tag{2}$$

If only the portions of $\Delta\mathbf{B}$ that are perpendicular to the background field are used in (2) we recover only the field-aligned portion of $\mathbf{J}$. In this case the perpendicular $\Delta\mathbf{B}$ components correspond to the sunward and duskward vectors.

Magnetometer data from different instruments are recorded at different altitudes, so care must be taken to ensure that each data point is comparable to the rest of the data

set. To do this, each data point is scaled to an altitude of 110 kilometers. This scaling only changes the magnitude of data, and not the relationships between magnetometer measurements and driving conditions.

Specific FAC mappings are generated by specifying a desired range of IMF clock angle, solar wind electric field, geomagnetic tilt angle, and solar radiative index values. The IMF clock angle is defined here as the angle between the B_y and B_z vectors, with 0° being positive B_z and no B_y, 90° being positive B_y and no B_z, and so forth. As mentioned in the Introduction, each of the solar indices was used independently of each other in this analysis. All measurements that were obtain at times that fell within the specific range of conditions are then selected, and used to generate a map of the distribution of the FAC.

A number of methods of correcting the problem of outlier points were implemented and tested, and it was decided for this analysis that the following method was the most effective. First, within any given selection of data, each data point was tagged with an identifier that showed which hemispheric pass it was associated with. Then, the maximum $\Delta\mathbf{B}$ magnitude from each set of points with the same identifier were determined and saved. The mean and standard deviation for these maximums were then determined. Next, each point with an identifier that contained a maximum that was greater than a chosen number of standard deviations from the mean was removed from the set of data based on the assumption that if one point in the pass was somehow corrupted that the entire pass was not trustworthy. Once these points were removed the process of finding maximums and removing sets of points that were outside the chosen standard deviations was repeated until either no data points were removed or a maximum number of iterations was reached. In this analysis, the standard deviation limiter was chosen to be 6σ and the maximum

number of iterations was chosen to be 10, although this process rarely went more than 3 iterations. In practice, this point removal process removed less than one percent of the data from each selection.

The distribution of the magnetic field over the polar cap is determined by spherical cap harmonic analysis (SCHA), such that

$$\Delta B(\lambda,\varphi) = \sum_{l=0}^{19} \sum_{m=0}^{min(l,3)} (A_{lm}\cos m\varphi + B_{lm}\sin m\varphi) P^m_{n_l(m)}(\cos\lambda), \tag{3}$$

where φ is the magnetic local time, λ is the co-latitude, $P^m_{n_l(m)}$ is the associated Legendre function, and A_{lm} and B_{lm} are the spherical harmonic coefficients that ultimately determine the two-dimensional structure [*Haines*, 1985]. The $\mathbf{\Delta B}$ solved in this way is separate for each component sunward and dawnward, such that each direction has its own set of coefficients. The fitting was done using a least-squares error algorithm.

The function $n_l(m)$ provides a non-integer degree of Legendre polynomial where the function goes to 0 at a chosen low-latitude boundary. This function is dependent on both l and m. As discussed previously by [*Weimer*, 2005b], the degree of m is much less important compared to that of l, as increasing the degree of m adds numerical artifacts that detract from the results significantly. In this specific version of the model, associated Legendre functions $P^m_{n_l(m)}$ of degree $l \in [0, 19]$ and order $m \in [0, 3]$ are used to derive the fits. As previously noted in [*Weimer*, 2005b] high degrees of m are mostly negligible in this methodology, and it is instead more favorable to include higher degrees of l.

Previous models, such as *Weimer* [2005b], made use of Euler potential constructions in order to attempt to determine the field-aligned current densities over the polar cap. This methodology was used primarily because the magnetometer data available was only reliable in the cross-track direction, as opposed to both the cross-track and on-track

trajectories. The Ørsted, CHAMP, and Swarm missions have data that are both reliable and have high time resolutions in all vector components, and thus do not require the use of magnetic Euler potentials. Instead, the field-aligned current can be calculated directly from Ampere's Law. An example of the two direction (sunward and dawn-dusk) $\Delta\mathbf{B}$ fitting and the final FAC calculated from this fitting can be seen in Figure 2. In this plot and all others showing FAC maps, a positive current is defined as one flowing in the direction of the magnetic field. Each figure shows the northern hemisphere perspective, where the positive current is going downward into the polar cap.

4. Low-Latitude Boundary Fit

As the solar wind and IMF inputs grow stronger the lower latitude boundary of the Region 2 current system moves lower in latitude [*Clausen et al.*, 2012; *Carter et al.*, 2016]. By restricting the cap size of the SCHA fitting the amount of erroneous fitting done at lower latitudes can be reduced significantly, and the size of the area that is being modeled is able to expand and contract with changes in the IMF. A low-latitude boundary model was developed using a selection of binned fits. From these fits the lowest latitude points were determined by the locations where the Region 2 current systems went to zero. While in previous models this location was determined by manual inspection (such as in *Weimer* [2005b]), this version used the region identification and totaling routines described in the next section to determine these cutoff locations.

The low-latitude boundaries found were then fit using least-squares and a model was derived such that

$$\lambda_0 = \sum_{n=0}^{3} A_n f_n \tag{4}$$

where A_n is a coefficient multiplied by some function f_n, and λ_0 is the latitude in degrees referenced from the northern hemisphere. These functions were defined by

$$\begin{aligned} f_0 &= 1 \\ f_1 &= \cos\theta \\ f_2 &= E \\ f_3 &= E\cos\theta \end{aligned} \tag{5}$$

where θ is the IMF clock angle and E is a solar wind electric field function defined by

$$E = \frac{E_{SW}}{\sqrt{1+\left(\frac{E_{SW}}{12000}\right)^2}}. \tag{6}$$

E_{SW} in this equation is the solar wind electric field in units of $\mu V/m$. For the purposes of this investigation, the coefficients used for this fit were found to be

$$\begin{aligned} A_0 &= 64.557598 \\ A_1 &= 1.8349828 \\ A_2 &= -0.0012902127 \\ A_3 &= 0.00031268707 \end{aligned} \tag{7}$$

This proved to be an effective means of finding the lower latitude boundary of the FAC map, but had some problems during clock angles near 180°, where the midnight sector FAC was being cut off prematurely. This was corrected by lowering the latitude boundary by 3 degrees in latitude, which allowed for the entire structure to be resolved without significant numerical artifacts being included. A number of other conditions such as dipole tilt angle were incorporated in the development of this fitting, but were found

to be negligible compared to the IMF clock angle and solar wind electric field and were ultimately removed.

A previous empirical model had used a hybrid technique [*Weimer*, 2005a], that had a circular, low-latitude boundary that was offset from the pole, toward midnight. This offset was still included in the next version of the model, that first used SCHA methods [*Weimer*, 2005b], even though it was not actually required. The low-latitude boundary that is used in the present analysis does not include an offset from the pole.

5. Determination of Region Totals

Knowing the total amount of current moving through the polar cap is very useful for understanding its role in the larger magnetosphere-ionosphere system, but knowing how much current moves through distinct areas is ultimately desired, as each current region is generally considered to be related to different processes and regions in the magnetosphere. For example, an enhancement in the Region 2 current systems could be related to an enhancement in ring current, while an enhancement in Region 1 current systems may be more related to reconnection events or substorms [*Clausen et al.*, 2012; *Coxon et al.*, 2016; *Carter et al.*, 2016]. This problem has gathered more interest in recent years as our understanding of the current sources in the magnetosphere becomes clearer. The structure of the high latitude magnetic field is highly varied, with different magnetic footprints corresponding to different areas in the magnetosphere.

While the identification of the different FAC regions and the derivation of their totals may appear simple at first, in reality this task is much more difficult than it would seem. The reason for this difficulty is that the Region 1 and 2 currents, as well as Region 0, do not begin and end at fixed MLT boundaries, and these different regions often run together

at the boundary, or overlap with each other. Figure 3 shows examples of two such cases that elude a simple analysis, at IMF clock angles of 180 and 270 degrees.

Any algorithm also needs to be able to derive the varying MLT locations that separate the dawn and dusk sides. Deciding where the downward Region 1 on the dawn side ends and the upward Region 1 on the dusk side ends can be difficult to pin-point by visual inspection, and manual input should also be avoided as it may unintentionally bias the results. Recent attempts at solving this issue included using machine learning algorithms to automatically identify suitable regions [*Wiltberger et al.*, 2016]. We have developed our own methodology of determining the regions' boundaries, which is described in the following section.

Using a traditional definition of dawn and dusk, a line could be drawn between 0 and 12 MLT that divides the polar cap into two sides. This method is not applicable for field-aligned current maps, as the boundaries between regions of upward and downward current systems can shift across this line, depending on driving IMF conditions. In the description that follows, the boundaries between the "dawn" and "dusk" sides are more flexible, having positions that depend on the natural configuration of the current regions.

The method to determine the current region totals consists of three major components: FAC map sampling, peak current location, and region identification and totaling.

In the initial step, the polar FAC map is divided into 360 meridional slices, equally spaced in MLT, and each slice is further divided into pixels by latitude, at 1 degree steps. The spherical surface areas of all pixels are calculated for future use. Each point in each MLT slice is now considered the center of a pixel on the surface of a sphere, at a radius of 6371.2+110 km, which is where the FAC was evaluated. The current density in each

pixel is obtained from a set of spherical cap harmonic coefficients, which is multiplied by the area to derive the total current in each pixel.

Next, along each MLT slice, the algorithm looks for the maximum (absolute value) for each sign of positive and negative current, and both locations in each slice are saved for future use. We start with the assumption that these are the Region 1 current peaks. The boundary of these regions is then found by scanning upward and downward from each peak in latitude until a change in sign is found. This will later be referred to as the "peak determination step." If no change in sign is found along an MLT slice, then the algorithm carries over the last known peak location. While the positive Region 1 is generally identified with the dawn side, and the negative Region 1 with the dawn side, lists of the Region 1 maximum and boundary latitudes for both signs are initially kept for all 360 slices.

Using the highest latitude peak found in each MLT slice, a circle around the polar cap is fit. This circle that results from this fit is allowed to be offset from the pole, often shifted toward a lower latitude near midnight. Once this circular fit is found, the radius of the circle is expanded by 10.5 degrees in latitude to create a low latitude boundary for the region identification. The reason for this step is that the FAC maps that are generated by a series of spherical harmonics may have artificial oscillations at latitudes below the Region 2 current. These artifacts can confuse any search algorithm, as wherever the Region 1 and Region 2 have gaps the peak current may be found within such oscillations, particularly for Northward IMF. This bounding circle excludes some numerical fluctuations that may otherwise be labeled as regions of interest. After the bounding circle is determined, then the peak determination step is repeated. This leaves us with two lists of peak current

locations and the region boundaries, one for positive current and one for negative current, but only down to the limiting circle.

Starting with the high latitude Region 1 limit found in the peak determination step, the total FAC having the same sign is summed along the meridian, at each longitude step. The summation is done upward in latitude, and downward to the latitude of the bounding circle. This is done even if there is a separate region of current with a different sign within the same path, rather than stopping the summation where the other sign is encountered.

Since the previous steps found the total current for a each sign regardless of MLT location, we can now establish a separation of Region 1 and Region 2 systems. The two peaks, positive and negative, are compared for each MLT slice. The peak with a higher latitude is chosen to be the Region 1 system, and the peak with the lower latitude is chosen as the Region 2 system. Region 0 systems are found by starting at the upper latitude boundary of each Region 1 system, then summing the current upward toward the the pole.

At this point we have computed two sets of Region 0, 1, and 2 totals, for currents having signs associated with both "dawn" and "dusk," at all 360 MLT steps. In one set, Region 1 has positive current, and in the other set Region 1 is associated with negative current. The next step is to determine the MLT values that divide the dusk and dawn sides. At each MLT step the absolute values of Region 1 and Region 2 are now added for both sets, and these totals are then smoothed with a 1-hour MLT (15 step) moving average.

Two dividing boundaries between dawn and dusk regions are determined by where this total has a minimum, one evaluated in the range of 9 to 15 MLT (centered on noon), and the other evaluated at MLT values greater than 21 or less than 3 hours (centered on

midnight). After these two MLT boundaries are located, then the sums of the Region 0, 1, and 2 currents in each region are obtained for both the dawn and dusk sectors.

It has been observed on the maps that Region 0 current on the dusk side often appears as a continuation of Region 1 on the dawn side, and vice versa. An example of this situation is shown on the rightmost map of Figure 3. The total current at boundary between these regions is often observed on the maps to be nearly continuous, while in the initial results of this process it appeared that current could be missing across the boundary in a few cases. In order to improve the accuracy we added the following procedure before the MLT boundary location. At each MLT step, if the positive Region 0 total is found to be greater than the positive Region 1 total, then that total is copied to the Region 1 value, as in the final result it will be part of the dawn Region 1 system. Likewise, if the negative Region 0 has a greater absolute value than the negative Region 1, then that value is copied to the Region 1 sum.

The computational procedure described here resulted from a incremental process. The end result appears to be quite accurate and robust, and a useful tool for deriving the totals of the currents within each region.

6. FAC Response to Solar Flux Index Variations

With the new wealth of data it is now possible to reliably produce FAC maps for secondary solar parameters, such as solar flux index. By using a series of fits of data binned by IMF clock angle, solar wind electric field, geomagnetic tilt angle, and solar radiative index values, the FAC response to increasing solar flux index has been analyzed. These results focus on the northern hemisphere response.

Figures 4-9 in this section demonstrate the results of our analysis. The points in each plot show the total current in specific selections over a given FAC map, derived from our totaling routine. Each FAC map was derived using a constrained bin of input parameters between solar wind electric field, dipole tilt angle, solar flux index, and IMF clock angle. Each bin is selected such that the data is distinct from all other bins, and as such none of the bins overlap in any way. The solar wind electric field was determined by multiplying the magnitude of the solar wind magnetic field vector component in the B_y-B_z plane with the solar wind velocity.

Three ranges of dipole tilt were used for sorting the data: $21° \pm 10.5°$, $0° \pm 10.5°$, and $-21° \pm 10.5°$. In Figures 4 - 9 the lines that correspond to each range of dipole tilt angle are colored red, green, and blue respectively. Measurements taken while the solar wind electric field had a magnitude under 4 mV/m were used in all bins. The majority of data are within this range, and the data having higher electric field values were excluded. For the sorting of data by the solar indices, the center values of the flux indices and the widths of these bins were chosen such that all bins within a group had a similar number of points. The number of points in these bins was highly dependent of the IMF clock angle, and varied from approximately 197000 to 1500000 points.

In order to evaluate different trends in the data two numerical fits were made: a linear and an arctangent fit, both of which used least-squares method. The linear fit was a simple line, corresponding to $y = A + Bx$, where A and B are constants determined by the fitting. The arctangent fit was slightly more complex, corresponding to $y = A \arctan(B(x - x_0) + C$, where A, B and C are constants determined by the fitting. The beginning of the arctangent function is very linear, but rolls over and has a saturation-like

trend at higher values. In order to more properly fit this function to the data, a constant x_0 that changes with solar index was introduced. This allowed the arctangent function to better fit data near the lower portion of the solar index selection. In this case, x_0 is 65 for F_{10}, 40 for S_{10}, 60 for M_{10}, and 55 for Y_{10}. After each trend is fit, the trend with this highest correlation coefficient is plotted. The fitting and correlation coefficients are provided in a Tables 1-6.

Determining the error in a given field-aligned current map is very difficult, but a new method has been applied to attempt to give a relative error scaling to the data. To do this, the difference between each data point and the fit is squared, and then divided by the number of points. This can be mathematically represented by

$$Err_{\Delta B} = \frac{\sum_i^n (y_i - f_i)}{n} \tag{8}$$

where y_i is a given data point used in the fit, f_i is the fitted value at that point, and n is the total number of points in the fit. Data and error sums in the sunward and dawnward directions are treated separately, and will be referred to as $Err_{\Delta B,Sunward}$ and $Err_{\Delta B,Dawnward}$. The square root of these values it used as an average error over the entire fit.

We then treat these errors as if they were ΔB values, and attempt to derive a measurement of the error for the field-aligned current from them by taking $\frac{1}{\mu_0}(Err_{\Delta B,Dawnward} - Err_{\Delta B,Sunward})$. This error is then divided by the total area of all current regions to get an error per unit area. Finally, when presented in the plots the error is multiplied by the area of the current regions being displayed to scale it accordingly, to units of total current.

6.1. Variations Between Different IMF Clock Angles

Shown in Figure 4 is the total current found in Regions 0, 1, and 2, using the average of both dawn and dusk sectors, for four different IMF clock angles. The current of each sign (positive or negative) is added together, and then the absolute value of each of these sums is averaged. The total average current provides a view of the total current moving through the polar cap, and allows for comparison between changes in solar driving conditions. In this set of plots the IMF clock angle changes so that different IMF B_y and B_z conditions can be compared.

The most obvious result of these plots is that the changes in current between each seasonal tilt selection is similar between plots, consistent with recent findings [*Coxon et al.*, 2016]. Summer currents are stronger than equinox currents, which are stronger than winter currents. Further, the current strengthens as the clock angle moves toward 180° from 0°, which is consistent with the idea that highly negative B_z provides the strongest driving of current in the polar cap [*Carter et al.*, 2016]. Additionally, the highly B_y dominant clock angles (90° and 270°) display a very similar total average current over the entire polar cap.

Outside of the seasonal and IMF clock angle conditions, of note is the nonlinear relationship as the solar flux index increases. This nonlinearity becomes more evident as the clock angles moves toward 180°, where trends like the winter selections show a much more dramatic saturation-like effect as the solar index increases. This is further emphasized by the nonlinear fit of each set of data, where the correlation coefficients outlined in Table 1 are significantly higher for the arctangent fit than the linear fit.

If we suppose that the current saturation is related to a saturation in ionospheric conductivity, it would follow that there is some mechanism where high solar index (and by surrogate, high solar flux) does not allow for the conductivity to increase. For example, if we further suppose that the conductivity is directly related to the population of ionized atomic species in the ionosphere, then this saturation would be due to a reduction in ionized species production, or rather, an increase in the loss of ionized species.

Having a general overview of the current moving through the polar cap is useful, but having detailed analysis of the current flowing through distinct regions is also important. As expressed previously, different regions of current are generally associated with different parts of the greater magnetosphere. Shown in Figure 5 is the average of the current magnitude found in Region 1 in the dawn and dusk sectors. In this case, only the Region 1 portions of the current systems from Figure 4 have been shown.

Consistent with the results from the previous figure the seasonal variation in total current remains the same, with summer conditions having the strongest current relative to other seasons and winter conditions having the weakest. Again, as the IMF clock angle moves toward 180° the current systems strengthen as a whole, so much so that even the winter current systems during 180° IMF clock angle shown in subplot (c) are stronger than the summer current systems at 0° IMF clock angle in subplot (a).

The saturation-like response of the current with increasing solar flux index is very noticeable in this selection, particularly with respect to the leveling off at high solar flux index. This is further emphasized in the correlation coefficients presented in Table 2, which for subplots (b), (c), and (d) are quite high compared to their linear counterparts.

While Region 1 systems tend to be most dominant [*Ganushkina et al.*, 2015], Region 2 systems are also very important to the complete picture of the polar current flow. Shown in Figure 6 is the average of the current magnitude found in Region 2 in the dawn and dusk sectors. These plots resemble those shown previously, however the current between different seasonal selections does not differ nearly as much as Region 1. Instead, data points are much more tightly packed and in cases like subplot (a) and (b) seem to overlap. Further, the Region 2 current systems have about half of the current magnitude than the Region 1 summer systems do.

Subplots (a), (b), and (d) also shown a much more linear trend compared to that of Region 1 with very little variation in season. This is still somewhat ambiguous, however, as the correlation coefficients of the arctangent fit outlined in Table 3 are consistently higher. This could be the result of a very shallow nonlinear trend. Noteworthy, however, is the clarity of the nonlinear trend in subplot (c), where the IMF is highly southward.

Now, with the two most dominant current regions explored, we can now look toward the much more dynamic Region 0 system. Shown in Figure 7 is the average of the current magnitude found in Region 0 in the dawn and dusk sectors. Plot (c) shows very little current as expected, since southward IMF does not tend to have Region 0 current systems. The other three subplots, however, show very similar trends. Summer and equinox selections tend to show a nonlinear increase in current as the solar index increases, while the winter selections are highly linear. The slope of this fit is very small and the correlation coefficient (shown in Table 4) is very similar to that of the nonlinear trend, which may suggest that there is a nonlinear trend similar to the other seasonal selections that is not as strong.

Notably, the summer selections are stronger than the equinox selections, which are stronger than the winter selections, which mimics the same effect as the total current and the Region 1 current. This was much less evident in the Region 2 current systems but still showed the separation between seasons, especially in Figure 6 subplots (c) and (d). From this, it appears that the summer hemisphere draws current away from the winter hemisphere for at least Region 0 and Region 1 systems, if not the total field-aligned current over the entire polar cap.

While it may not seem so on the surface, the magnitude of the current systems in subplot (a) of Figure 7 is important to note. In previous plots it can be seen that the magnitude of current systems at 0° IMF clock angle are smaller than that of other IMF clock angles, but this is not the case for Region 0 systems. Instead, the magnitude of the current in for 0° IMF clock angle is very similar to the of 90° and 270° IMF clock angle.

Highly positive or negative B_y IMF conditions with B_z close to zero have a very significant Region 0 enhancement, which is either positive or negative depending on clock angle. While the Region 1 current is still clearly dominant in the total current over the polar cap, the Region 0 enhancement is very clearly dynamic and in the case of summer tilts comparable to the total current in the Region 2 system.

6.2. Variations Between Solar Indices

With the context of the figures in the previous section, we can now compare current strengths between different solar index selections. Shown in Figure 8 is the average of the current magnitude found in Regions 0, 1, and 2 in the dawn and dusk sectors at a clock angle of 180°. Selections using different solar index plots are shown, with subplot (a)

showing F_{10}, subplot (b) showing M_{10}, subplot (c) showing S_{10}, and subplot (d) showing Y_{10}.

As seen in the previous F_{10} plots, subplots (a), (b), and (c) show very nonlinear trends and saturation-like effects as the solar index value increases. Surprisingly, the response to the Y_{10} index shown in subplot (d) does not show this saturation effect and instead remains almost completely linear. Previously it was mentioned that many of the linear trends may just be very shallow nonlinear response, but in this case that may not be true. While the correlation coefficients of the linear and arctangent fits shown in Table 5 are both very similar, the slope of these trends are much higher than those seen previously, such as Figure 6 subplots (a), (b), and (d), and all of the plots in Figure 7.

This may be due to how the Y_{10} index is constructed. The F_{10}, S_{10}, and M_{10} indices can be related to absorption processes in the upper ionosphere. In particular, the S_{10} index is primarily related to the F-region of the ionosphere, and the M_{10} index is primarily related to the E-region. Y_{10}, however, is more directly related to the lower ionosphere in the D-region [*Tobiska et al.*, 2008; *Bowman et al.*, 2008].

As described in the introduction to this paper, the Y_{10} index is a mixture of a solar X-ray measurement and a series of Lyman-α measurements. The X-ray portion of the index is dominantly weighted during solar maximum, while the Lyman-α measurements are dominantly weighted during solar minimum. This weighting is very important, as most of the data from the Ørsted, CHAMP, and Swarm missions was recorded during or near solar maximum, particularly with respect to the Ørsted and Swarm missions. As noted by *Bowman et al.* [2008], the X-ray flux used in this index primarily ionizes the D-region of the ionosphere, which is notably much lower in altitude compared to the

magnetometer measurements used to derive these current fits in this paper. As such, it may be that the X-ray input does little to effect the field-aligned currents, and as such is not effected by the same saturation mechanism that is apparent in the other three solar indices.

Shown in Figure 9 is the average of the current magnitude found in Regions 0 and 1 in the dawn and dusk sectors at a clock angle of 90°. The seasonal relationship between summer, equinox, and winter selections remains consistent between different solar indices. Similar to Figure 8, there appears to be fairly consistent nonlinear trend with increasing solar index, which is reinforced by the correlation coefficients shown in Table 6. Again, the Y_{10} solar index appears to be an exception here, showing a very linear trend compared to the other three.

7. Summary

Further developments have been made to improve methods for developing field-aligned currents using satellite based high-latitude magnetometer measurements. In addition to the fitting algorithm improvements, a FAC region identification and totaling routine has been developed. Using these improvements, a number of selections based on solar radiative indices and seasonal tilts were made to better understand the effects of solar radiation on the FAC structure. It was found that there are nonlinear relationships between increasing solar flux index and total current for F_{10}, S_{10}, and M_{10} solar flux indices. Surprisingly, this is not the case for the Y_{10} index, where the response is highly linear. The different response to the Y_{10} index may be due to its association with wavelengths that are absorbed in the D-region of the ionosphere, below the altitude where FACs tend to close. As all of the various solar indices have some degree of correlation with each other, it appears that

the Y_{10} index is simply acting as a proxy for energy at other wavelengths that do produce a linear response in the conductivity and currents. In addition, the summer selections have consistently more current than winter selections in Regions 0 and 1, suggesting that current is drawn away from the winter hemisphere to the summer hemisphere.

Acknowledgments. This work is supported by National Science Foundation grant AGS-1303116 to Virginia Tech. The Ørsted data are freely available at ftp://ftp.spacecenter.dk/data/magnetic-satellites/Orsted/, provided by the National Space Institute at the Technical University of Denmark (DTU Space). The authors would like to thank Dr. Herman Lühr for providing the CHAMP magnetometer data. The CHAMP data are available from the Information System and Data Center for Geoscientific Data, at GFZ German Research Centre for Geosciences, which is available at http://isdc-old.gfz-potsdam.de/. The CHAMP mission was sponsored by the Space Agency of the German Aerospace Center (DLR) through funds of the Federal Ministry of Economics and Technology. Swarm data were obtained from the European Space Agency, available at https://earth.esa.int/web/guest/missions/esa-operational-eo-missions/swarm. The level 2 ACE data can be obtained from the NASA archives at ftp://cdaweb.gsfc.nasa.gov/pub/data/ace. The solar indices, found at http://sol.spacenvironment.net/~JB2008/indices.html, are provided by Space Environment Technologies.

References

Bolduc, L. (2002), GIC observations and studies in the hydro-quebec power system, *J. Atmos. Sol.-Terr. Phys.*, *64*, 1793.

Boteler, D. H., R. J. Pirjola, and H. Nevanlinna (1998), The effects of geomagnetic disturbances on electrical systems at the Earth's surface, *Adv. Space Res.*, *22*, 17.

Bowman, B. R., W. K. Tobiska, F. A. Marcos, C. Y. Huang, C. S. Lin, and W. J. Burke (2008), A new empirical thermospheric density model JB2008 using new solar and geomagnetic indices, in *AIAA 2008-6438*, AIAA Astrodynamics Conference, Honolulu, HI.

Carter, J. A., S. E. Milan, J. C. Coxon, M.-T. Walach, and B. J. Anderson (2016), Average field-aligned current configuration parameterized by solar wind conditions, *Journal of Geophysical Research: Space Physics*, *121*(2), 1294–1307, doi:10.1002/2015JA021567, 2015JA021567.

Clausen, L. B. N., J. B. H. Baker, J. M. Ruohoniemi, S. E. Milan, and B. J. Anderson (2012), Dynamics of the region 1 birkeland current oval derived from the active magnetosphere and planetary electrodynamics response experiment (ampere), *Journal of Geophysical Research: Space Physics*, *117*(A6), n/a–n/a, doi:10.1029/2012JA017666, a06233.

Cowley, S. (2000), Magnetosphere-ionosphere interactions: A tutorial review, *Magnetospheric current systems*, pp. 91–106.

Coxon, J. C., S. E. Milan, J. A. Carter, L. B. N. Clausen, B. J. Anderson, and H. Korth (2016), Seasonal and diurnal variations in ampere observations of the birkeland currents compared to modeled results, *Journal of Geophysical Research: Space Physics*, *121*(5), 4027–4040, doi:10.1002/2015JA022050, 2015JA022050.

Ganushkina, N. Y., M. W. Liemohn, S. Dubyagin, I. A. Daglis, I. Dandouras, D. L. De Zeeuw, Y. Ebihara, R. Ilie, R. Katus, M. Kubyshkina, S. E. Milan, S. Ohtani, N. Ost-

gaard, J. P. Reistad, P. Tenfjord, F. Toffoletto, S. Zaharia, and O. Amariutei (2015), Defining and resolving current systems in geospace, *Annales Geophysicae*, *33*(11), 1369–1402, doi:10.5194/angeo-33-1369-2015.

Gummow, R. A. (2002), GIC effects on pipeline corrosion control systems, *J. Atmos. Sol.-Terr. Phys.*, *64*, 1755.

Haines, G. V. (1985), Spherical cap harmonic analysis, *J. Geophys. Res.*, *90*(B3), 2583.

Iijima, T., and T. A. Potemra (1976a), The amplitude distribution of field aligned currents at northern high latitudes observed by Triad, *J. Geophys. Res.*, *81*, 2165–2174.

Iijima, T., and T. A. Potemra (1976b), Field-aligned currents in the dayside cusp observed by triad, *Journal of Geophysical Research*, *81*(34), 5971–5979, doi: 10.1029/JA081i034p05971.

ISO 14222 (2013), Space environment (natural and artificial) earth upper atmosphere, *International Organization for Standardization, Geneva*.

Lanzerotti, L. J., and G. P. Gregori (1986), Telluric currents: the natural environment and interactions with man-made systems, the earth's electrical environment, in *Studies in geophysics*, edited by E. P. Krider, R. G. Roble, and T. M. Usselman, pp. 232–257, National Academy Press, Washington, D.C.

Olsen, N., E. Friis-Christensen, R. Floberghagen, P. Alken, C. D. Beggan, A. Chulliat, E. Doornbos, J. T. da Encarnação, B. Hamilton, G. Hulot, J. van den IJssel, A. Kuvshinov, V. Lesur, H. Lühr, S. Macmillan, S. Maus, M. Noja, P. E. H. Olsen, J. Park, G. Plank, C. Püthe, J. Rauberg, P. Ritter, M. Rother, T. J. Sabaka, R. Schachtschneider, O. Sirol, C. Stolle, E. Thébault, A. W. P. Thomson, L. Tøffner-Clausen, J. Velímský, P. Vigneron, and P. N. Visser (2013), The Swarm satellite con-

stellation application and research facility (SCARF) and Swarm data products, *Earth, Planets and Space*, *65*(11), 1189–1200, doi:10.5047/eps.2013.07.001.

Rees, D., B. R. Bowman, and W. K. Tobiska (2012), Earth's upper atmosphere above 120 km., in *39th COSPAR Scientific Assembly*, vol. 39, p. 1601.

Reigber, C., H. Lühr, and P. Schwintzer (2002), Champ mission status, *Advances in Space Research*, *30*(2), 129–134.

Richmond, A. D. (1995), Ionospheric electrodynamics using magnetic apex coordinates, *J. Geomag. Geoelectr.*, *47*, 191.

Thomsen, P. L., and F. Hansen (1999), Danish ørsted mission in-orbit experiences and status of the danish small satellite programme, in *Annual AIAA/Utah State University Conference on Small Satellites, 13 th, Logan, UT*.

Tobiska, W. K., S. D. Bouwer, and B. R. Bowman (2008), The development of new solar indices for use in thermospheric density modeling, *J. Atmos. Sol. Terr. Phys.*, *70*, 803.

Tobiska, W. K., B. R. Bowman, and S. D. Bouwer (2012), Cospar international reference atmosphere, chapter 4 - solar and geomagnetic indices for thermospheric density models, *Tech. rep.*

VanZandt, T. E., W. L. Clark, and J. M. Warnock (1972), Magnetic apex coordinates: A magnetic coordinate system for the ionospheric f_2 layer, *J. Geophys. Res.*, *77*, 2406.

Weimer, D. R. (2005a), Improved ionospheric electrodynamic models and application to calculating Joule heating rates, *J. Geophys. Res.*, *110*, A05306, doi: 10.1029/2004JA010884.

Weimer, D. R. (2005b), Predicting surface geomagnetic variations using ionospheric electrodynamic models, *J. Geophys. Res.*, *110*, A12307, doi:10.1029/2005JA011270.

Wiltberger, M., E. J. Rigler, V. Merkin, and J. G. Lyon (2016), Structure of high latitude currents in magnetosphere-ionosphere models, *Space Science Reviews*, pp. 1–24, doi: 10.1007/s11214-016-0271-2.

Table 1. Linear and arctangent correlation coefficients associated with Figure 4. Only the fit with the highest correlation coefficient is plotted in the corresponding figure, and has been made bold in the table.

Subplot	Tilt	Linear	Arctangent	Subplot	Tilt	Linear	Arctangent
a (0°)	21.5° (red)	0.75599	**0.97428**	b (90°)	21.5° (red)	0.86582	**0.98553**
	0° (green)	0.49262	**0.84712**		0° (green)	0.86328	**0.94352**
	−21.5° (blue)	0.57607	**0.80940**		−21.5° (blue)	0.69082	**0.90474**
c (180°)	21.5° (red)	0.72058	**0.95270**	d (270°)	21.5° (red)	0.86572	**0.98050**
	0° (green)	0.75247	**0.93319**		0° (green)	0.79908	**0.97601**
	−21.5° (blue)	0.76638	**0.98112**		−21.5° (blue)	0.61693	**0.89137**

Table 2. As in Table 1, but associated with Figure 5.

Subplot	Tilt	Linear	Arctangent	Subplot	Tilt	Linear	Arctangent
	21.5° (red)	0.64580	**0.93594**		21.5° (red)	0.85804	**0.99062**
a (0°)	0° (green)	0.29886	**0.68278**	b (90°)	0° (green)	0.81965	**0.94604**
	−21.5° (blue)	0.29456	**0.75058**		−21.5° (blue)	0.56047	**0.92036**
	21.5° (red)	0.76174	**0.97178**		21.5° (red)	0.86161	**0.96955**
c (180°)	0° (green)	0.74537	**0.92163**	d (270°)	0° (green)	0.75559	**0.96322**
	−21.5° (blue)	0.68861	**0.98807**		−21.5° (blue)	0.58507	**0.91134**

Table 3. As in Table 1, but associated with Figure 6.

Subplot	Tilt	Linear	Arctangent	Subplot	Tilt	Linear	Arctangent
	21.5° (red)	0.66658	**0.75521**		21.5° (red)	0.93758	**0.96344**
a (0°)	0° (green)	0.38750	**0.77789**	b (90°)	0° (green)	0.87926	**0.92471**
	−21.5° (blue)	0.39831	**0.56175**		−21.5° (blue)	0.78447	**0.87896**
	21.5° (red)	0.64271	**0.90611**		21.5° (red)	0.85679	**0.91536**
c (180°)	0° (green)	0.79282	**0.95044**	d (270°)	0° (green)	0.80738	**0.98057**
	−21.5° (blue)	0.83844	**0.96939**		−21.5° (blue)	0.56513	**0.78855**

Table 4. As in Table 1, but associated with Figure 7.

Subplot	Tilt	Linear	Arctangent	Subplot	Tilt	Linear	Arctangent
	21.5° (red)	0.72596	**0.92587**		21.5° (red)	0.72800	**0.93484**
a (0°)	0° (green)	0.75714	**0.87532**	b (90°)	0° (green)	**0.90559**	0.72912
	−21.5° (blue)	**0.91771**	0.47167		−21.5° (blue)	**0.76679**	0.51097
	21.5° (red)	0.00389	**0.03366**		21.5° (red)	0.67931	**0.89210**
c (180°)	0° (green)	0.08554	**0.39619**	d (270°)	0° (green)	0.88395	**0.94583**
	−21.5° (blue)	**0.48499**	0.36993		−21.5° (blue)	0.67336	**0.79456**

Table 5. As in Table 1, but associated with Figure 8.

Subplot	Tilt	Linear	Arctangent	Subplot	Tilt	Linear	Arctangent
	21.5° (red)	0.72058	**0.95357**		21.5° (red)	0.87356	**0.99349**
a (F_{10})	0° (green)	0.75247	**0.93348**	b (M_{10})	0° (green)	0.80466	**0.94685**
	−21.5° (blue)	0.76638	**0.98112**		−21.5° (blue)	0.85967	**0.96084**
	21.5° (red)	0.77124	**0.94362**		21.5° (red)	0.96595	**0.98382**
c (S_{10})	0° (green)	0.89508	**0.97174**	d (Y_{10})	0° (green)	**0.92728**	0.92640
	−21.5° (blue)	0.80243	**0.95786**		−21.5° (blue)	0.95219	**0.96808**

Table 6. As in Table 1, but associated with Figure 9.

Subplot	Tilt	Linear	Arctangent	Subplot	Tilt	Linear	Arctangent
	21.5° (red)	0.86582	**0.98553**		21.5° (red)	0.92182	**0.96294**
a (F_{10})	0° (green)	0.86328	**0.94360**	b (M_{10})	0° (green)	0.86009	**0.92812**
	−21.5° (blue)	0.69082	**0.90506**		−21.5° (blue)	0.83649	**0.90974**
	21.5° (red)	0.79754	**0.92059**		21.5° (red)	0.97906	**0.98447**
c (S_{10})	0° (green)	0.85062	**0.96351**	d (Y_{10})	0° (green)	0.93736	**0.94654**
	−21.5° (blue)	0.91822	**0.97447**		−21.5° (blue)	**0.92164**	0.78742

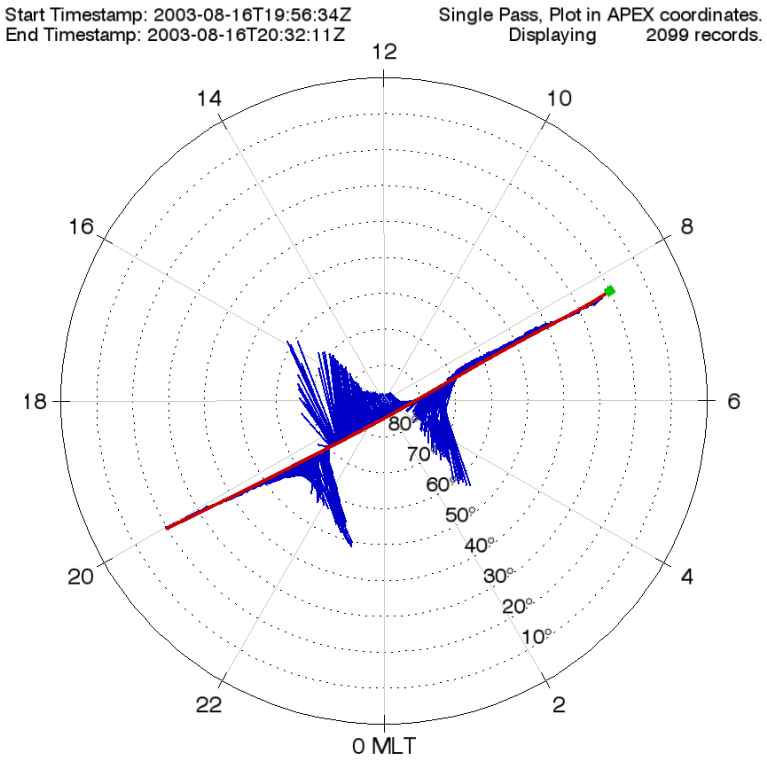

Figure 1. An example of a processed CHAMP magnetometer pass in corrected geomagnetic coordinates. The satellite's path is shown in red, and $\Delta\mathbf{B}$ data is shown in blue. The start of the pass is noted by a green square.

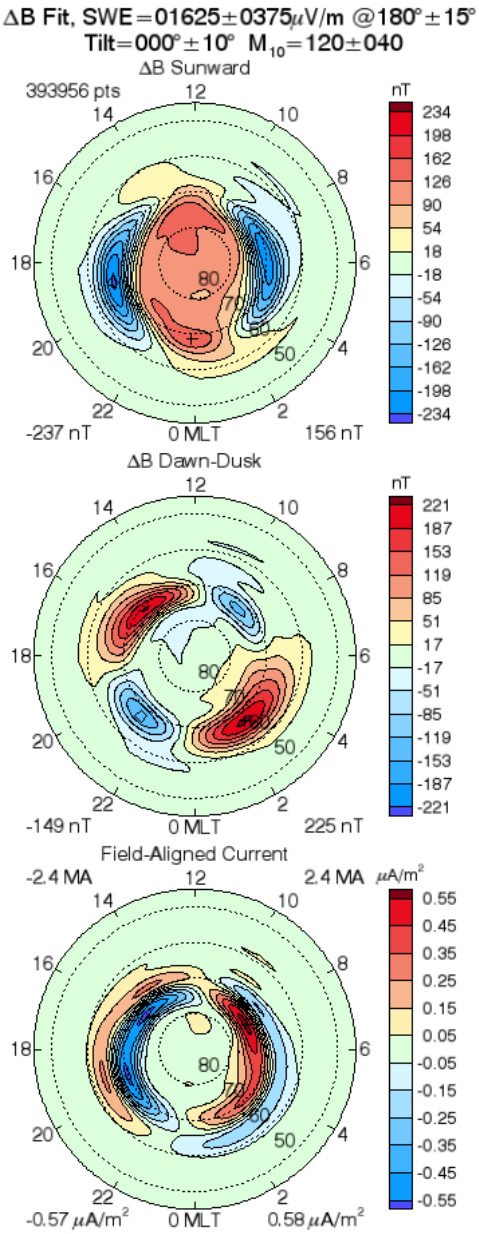

Figure 2. An example of **ΔB** fitting in the sunward and dawn-dusk directions, and the resulting field-aligned current derived from Ampere's Law. The minimum and maximum values in each plot are indicated in the lower left and right corners, respectively. The totals of the negative and positive FAC are shown in the upper left and right corners of the bottom plot, respectively.

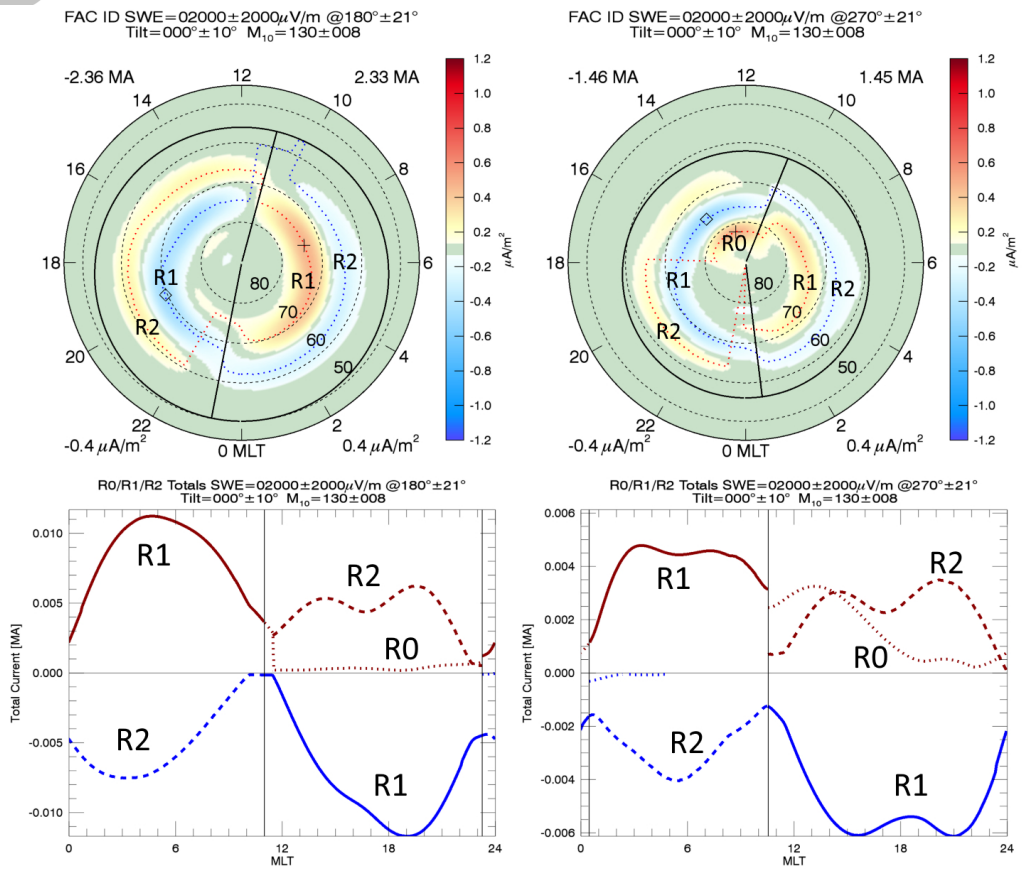

Figure 3. Two example current maps demonstrating the region identification and totaling. Two IMF clock angles are shown, at 180° ± 22.5° and 270° ± 22.5°. Otherwise, each system uses the same parameter bins, with the solar wind electric field in the range of 0 to 4 mV/m, 0° ± 10.5° dipole tilt angle, and solar flux index M_{10} 130 sfu ± 8 sfu. Dotted lines in the current maps show the maximum or minimum of the current in a given MLT slice, where red is the maximum (downward) and blue is the minimum (upward) current. The lower boundary is denoted by a solid black circle, and the dawn-dusk separation is denoted by solid black lines. Below the circular maps of the polar cap current systems is a plot of total current in that current map. Solid lines denote Region 1 (R1) current systems, dashes lines denote Region 2 (R2) current systems, and dotted lines denote Region 0 (R0) current systems. Positive (downward) currents are shown in red and negative (upward) currents are shown in blue. The difference in upward and downward current is very small, and may be caused by a number of factors that are difficult to attribute. They may be due to modeling errors, physical processes, or data errors. Minimum and maximum current values are indicated in the lower left and right corners of each map, while the total of the negative and positive currents are shown in the upper corners.

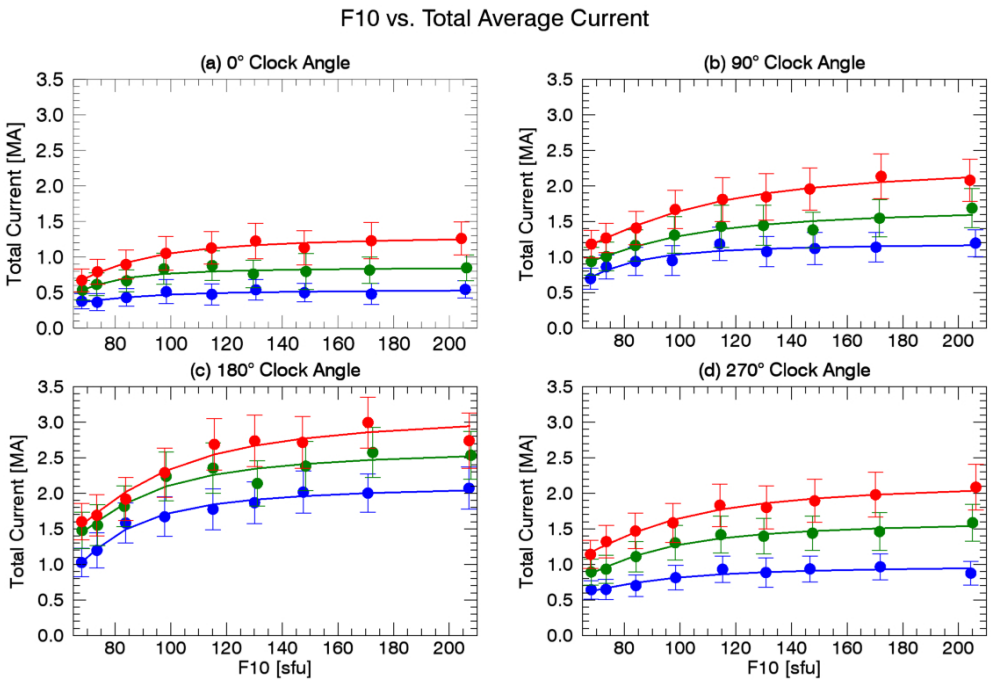

Figure 4. The average of the current magnitude found in Regions 0, 1, and 2 in the dawn and dusk sectors. Four clock angle selections are shown: (a) 0°, (b) 90°, (c) 180°, and (d) 270°. The solar flux in units of W m^{-2} Hz^{-1} (sfu) is shown on the x-axis of each plot, and the total current in units of MA is shown on the y-axis. Within each subplot, seasonal selections are also shown, with summer in red, equinox in green, and winter in blue.

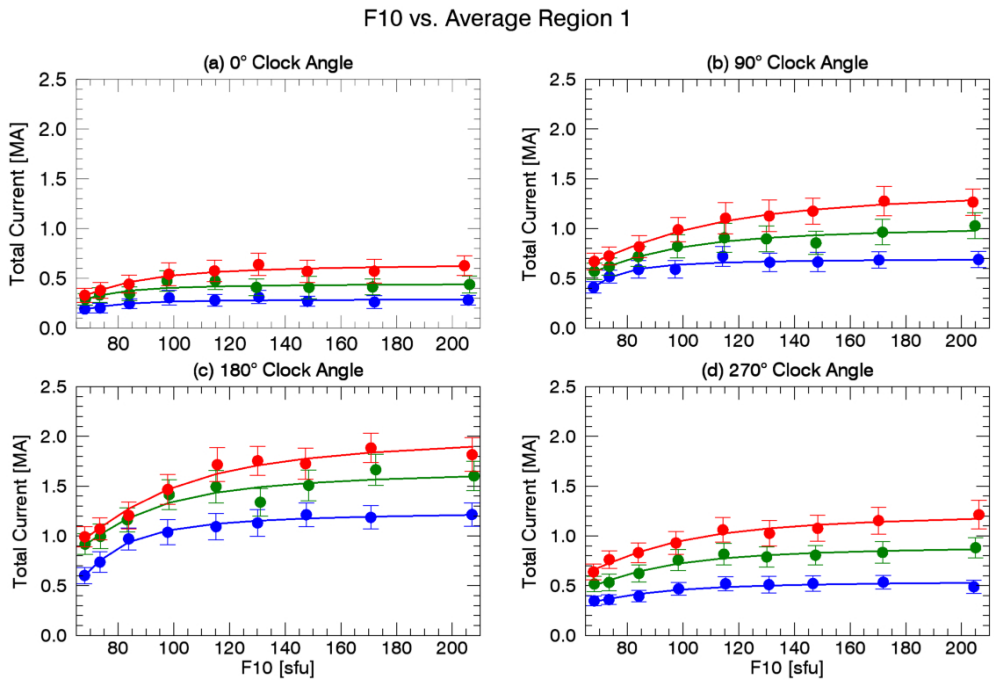

Figure 5. The average of the current magnitude found in Region 1 in the dawn and dusk sectors. Four clock angle selections are shown: (a) 0°, (b) 90°, (c) 180°, and (d) 270°. The solar flux in units of W m^{-2} Hz^{-1} (sfu) is shown on the x-axis of each plot, and the total current in units of MA is shown on the y-axis. Within each subplot, seasonal selections are also shown, with summer in red, equinox in green, and winter in blue.

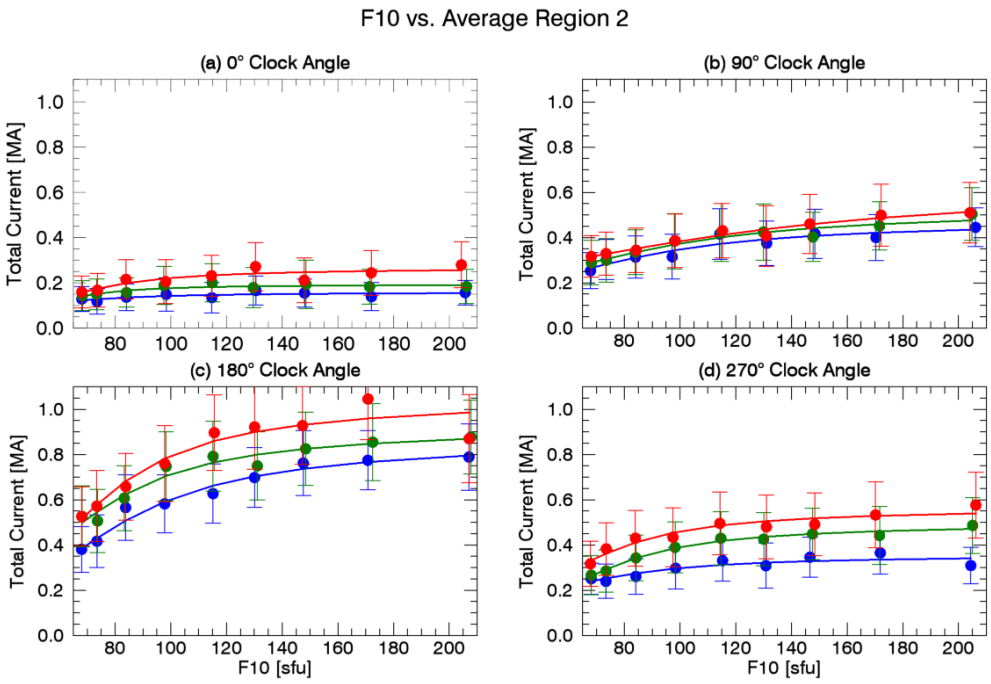

Figure 6. The average of the current magnitude found in Region 2 in the dawn and dusk sectors. Four clock angle selections are shown: (a) 0°, (b) 90°, (c) 180°, and (d) 270°. The solar flux in units of W m^{-2} Hz^{-1} (sfu) is shown on the x-axis of each plot, and the total current in units of MA is shown on the y-axis. Within each subplot, seasonal selections are also shown, with summer in red, equinox in green, and winter in blue.

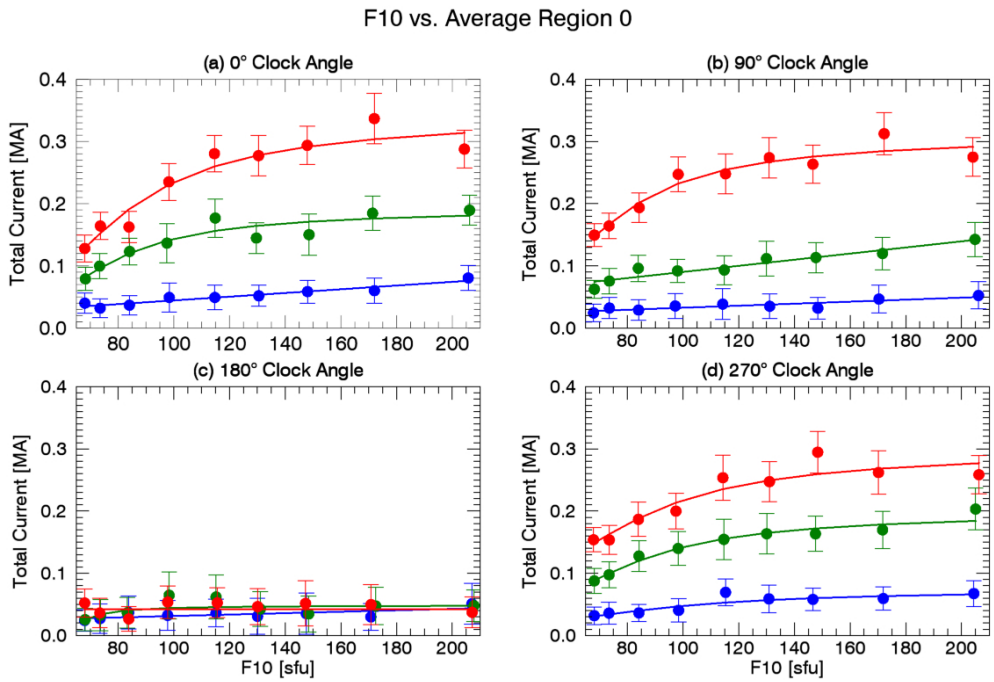

Figure 7. The average of the current magnitude found in Region 0 in the dawn and dusk sectors. Four clock angle selections are shown: (a) 0°, (b) 90°, (c) 180°, and (d) 270°. The solar flux in units of W m^{-2} Hz^{-1} (sfu) is shown on the x-axis of each plot, and the total current in units of MA is shown on the y-axis. Within each subplot, seasonal selections are also shown, with summer in red, equinox in green, and winter in blue.

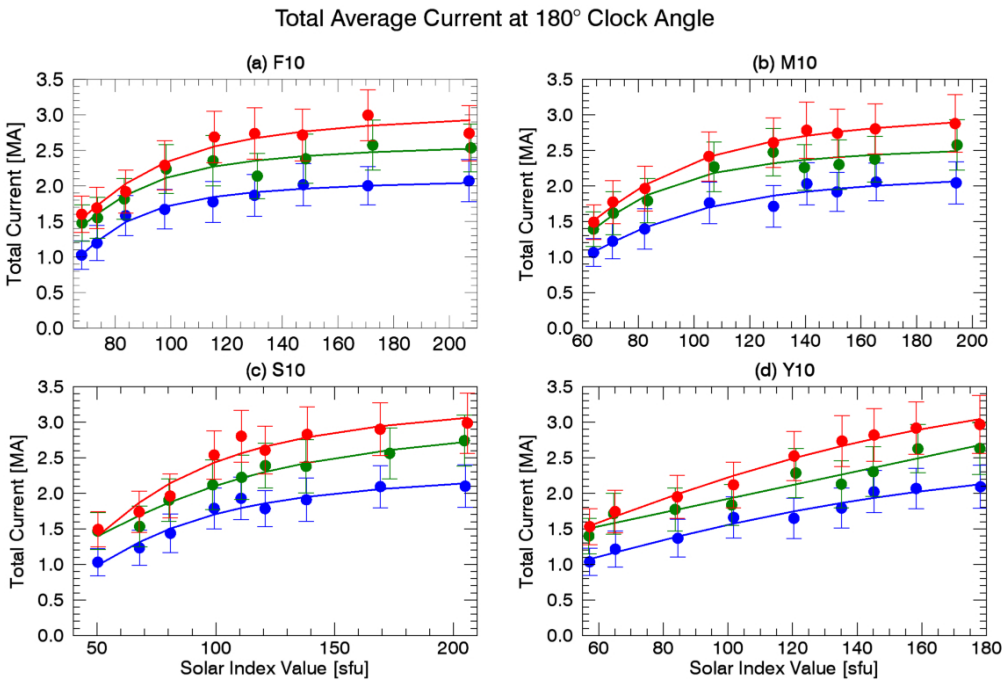

Figure 8. The average of the current magnitude found in Regions 0, 1, and 2 in the dawn and dusk sectors. Four solar index selections are shown: (a) F_{10}, (b) M_{10}, (c) S_{10}, and (d) Y_{10}. The solar flux in units of W m^{-2} Hz^{-1} (sfu) is shown on the x-axis of each plot, and the total current in units of MA is shown on the y-axis. Within each subplot, seasonal selections are also shown, with summer in red, equinox in green, and winter in blue.

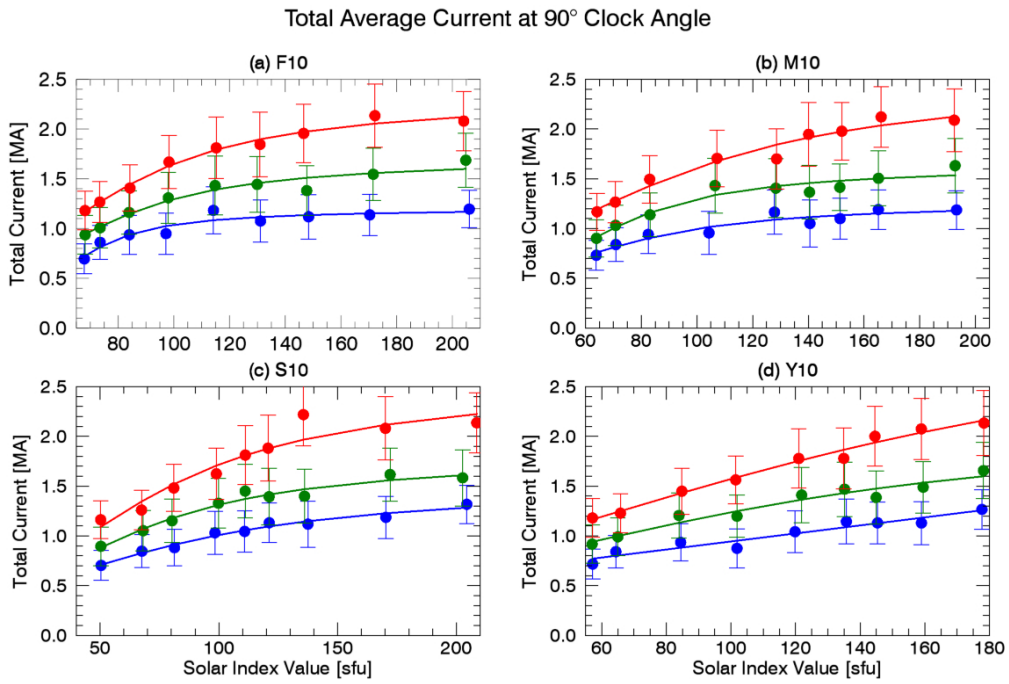

Figure 9. The average of the current magnitude found in Regions 0, 1, and 2 in the dawn and dusk sectors. Four solar index selections are shown: (a) F_{10}, (b) M_{10}, (c) S_{10}, and (d) Y_{10}. The solar flux in units of W m^{-2} Hz^{-1} (sfu) is shown on the x-axis of each plot, and the total current in units of MA is shown on the y-axis. Within each subplot, seasonal selections are also shown, with summer in red, equinox in green, and winter in blue.